(Received 21 September 2025, Accepted 13 November 2025, Scheduled 5 December 2025)

# Study on the Misalignment Tolerance of Dynamic Wireless Charging System for Smart Rail Vehicles Based on Reverse Series Multilayer Interactive Coil Structures

Yonghong Long[1], Jialin Zou[1], Zhongqi Li[1,2], Chenxi Zhang[1], and Junjun Li[1,*]

[1] College of Transportation and Electrical Engineering, Hunan University of Technology, Zhuzhou 412000, China
[2] College of Electrical and Information Engineering, Hunan University, Changsha 412008, China

**ABSTRACT:** In the dynamic wireless charging system for intelligent rail vehicles, coil misalignment causes mutual inductance fluctuations, resulting in significant output power variations and low transmission efficiency. To address this, a reverse series multilayer interactive coil (RSMIC) structure is proposed. This configuration enhances mutual interaction between coils by incorporating reverse-wound coils, symmetrical DD coils, and magnetic cores, thereby improving the system's misalignment tolerance. First, the structural characteristics of the RSMIC coils are introduced, and their mutual inductance patterns are analyzed. Next, based on a vector magnetic potential mutual inductance calculation method, coil and core parameters are optimized using a mutual inductance fluctuation minimization strategy to achieve quasi-constant mutual inductance and improved transmission efficiency. Ultimately, a wireless charging system was developed according to the optimization outcomes, and its accuracy was validated via both simulation and practical tests. The findings show that even when the ferrite-aided RSMIC coil is misaligned by up to 55% (184.8 mm) of the transmitter coil's external length, the highest variation rate in mutual inductance remains as low as 4.79%, enabling the system to attain a transfer efficiency of 97.35%.

## 1. INTRODUCTION

Magnetically-Coupled Resonant Wireless Power Transfer (MCR-WPT) technology has made significant strides in recent years, offering distinct advantages over traditional contact-based charging solutions: eliminating physical contact reduces mechanical wear while enhancing charging convenience and safety. This technology has achieved large-scale application across multiple sectors including electrified transportation systems, railway systems, implantable medical instruments, personal electronic products, and industrial apparatus [1–3]. Intelligent Rail Transit Vehicles (IRTVs), as a green and efficient public transportation solution, have garnered widespread attention. Utilizing dynamic wireless charging technology, they enable wireless energy transfer during operation, overcoming the limitations and inconveniences of traditional wired charging methods. Dynamic wireless charging primarily employs two modes: The segmented rail system divides the track into independent modules, dynamically activating power supply in corresponding zones based on vehicle position. This achieves over 90% efficiency and offers flexible scalability, making it the current mainstream solution [4–6]. This paper adopts the segmented rail power supply method, with its schematic shown in Figure 1.

In dynamic wireless charging systems, an inherent challenge in such systems is the positional displacement that occurs between the transmitting and receiving coils. This misalignment causes fluctuations in mutual inductance, which consequently compromises the overall efficiency and operational stability of the power transfer system. Innovations and optimizations in coil structures directly influence the system's misalignment tolerance. Therefore, exploring coil structures with superior misalignment resistance is a critical research direction [7–10].

Magnetic coupling coils can be categorized into single-coil and multi-coil structures. Single-coil designs include circular, rectangular, and other polygonal configurations. Conventional single-coil designs demonstrate a notable decrease in effective coupling area under misalignment conditions. Particularly when the misalignment exceeds 50% of the transmitter coil's outer diameter, the direct magnetic flux sharply decreases while negative magnetic flux is generated. This results in a drastic drop in mutual inductance, making it difficult to meet the demands of dynamic scenarios [11, 12].

In contrast, multi-coil structures form magnetic field interference networks through spatial superposition: their superimposed magnetic fields increase the effective coupling area by approximately 2–3 times, while the dynamic equilibrium mechanism of mutual inductance between coils compensates for

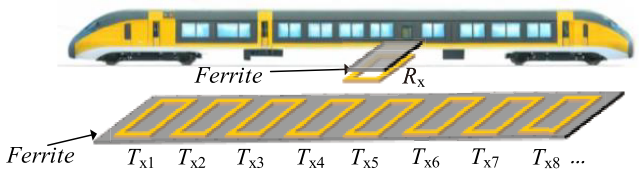


**FIGURE 1.** Schematic diagram of dynamic wireless charging for smart rail train.

* Corresponding author: Junjun Li (lijunjun@hut.edu.cn).

magnetic flux variations caused by displacement. The DD-type magnetic coupler [13] proposed earlier by the University of Auckland team in New Zealand enhances longitudinal offset resistance by forming a closed magnetic flux path through series-connected dual coils, but suffers from a magnetic field null zone issue. The subsequently improved DDQ structure [14] orthogonally superimposed a Q-coil onto the DD coil, eliminating the zero region while further enhancing multi-directional offset resistance, but at increased cost and complexity. To reduce costs, the team further designed a bipolar plate (BP) structure [15] suitable for automatic guided vehicles (AGVs), employing a bipolar plate layout to maintain high coupling efficiency under wide lateral offsets, though its performance falls short of DDQ. Building upon this, tripolar pad (TP) structure [16] enhances anti-offset and anti-deflection capabilities by selectively energizing different coils, while the Tai Chi coil [17] further improves coupling coefficients and misalignment tolerance through optimized coil topology. In other research, Quadruple D (QD) coils [18] enhance offset resistance through decoupled design, but their weak central magnetic field issue is resolved in the improved QDS structure [19] by superimposing S-coils. Additionally, dual-receiver coil systems [20] achieve high misalignment tolerance through decoupled parallel rectification, while triple-coil systems [21] expand multidirectional offset resistance by incorporating a reverse-connected third coil. Hexagonal array coils [22] enhance system robustness through flexible combination and switching strategies. Asymmetric reverse-series-connected (ARSC) coils [23] achieve low mutual inductance fluctuation rates by inserting a rectangular coil in reverse series between isotropic DD coils, with parameters optimized using a double Fourier transform analytical method. The hybrid compensation topology of four rectangular orthogonal coils [24] achieves full-angle anti-drift capability through multi-coil coordination. While dual-layer orthogonal DD coils [25] exhibit strong anti-drift performance, they suffer from relatively low coupling coefficients and inefficient transmission. Inverse series coil (ISC) mitigate mutual inductance variation via three coils in positive-negative series, with low fluctuation for misalignment within half of the transmitting coil's side length [26]. Flat solenoid paired with inductor-capacitor-capacitor-series (LCC/S) compensation topology and Buck converter, maintains stable efficiency and constant voltage under specific transmission distance and lateral misalignment [27].

Although the aforementioned studies have made significant progress in improving the offset tolerance of wireless power transfer systems, certain limitations remain. For example, some structures are complex with high design costs, whereas other approaches only suit specific scenarios and lack universality. To overcome these challenges, this paper proposes a dynamic wireless charging system for smart rail transit trains based on a reverse-series multi-layer interactive coil (RSMIC) structure. This structure enhances coil interaction via reverse-wound coils, symmetrical DD coils, and magnetic cores, ensuring stable mutual inductance under misalignment. The proposed RSMIC has advantages of simplicity, low design cost, and strong universality, fitting dynamic wireless charging systems in diverse scenarios.

Subsequent sections will focus on the design, optimization, and experimental validation of the RSMIC structure. First, a comprehensive explanation of the operational mechanism and design foundations of the RSMIC configuration will be provided. Second, coil and core dimensions will be optimized using a strategy to minimize mutual inductance fluctuations. Finally, an experimental platform will be constructed to validate the RSMIC structure's offset tolerance performance.

## 2. RSMIC STRUCTURE

### 2.1. Calculation Method for Rectangular Coil Mutual Inductance

To support the coupling coil design and enhance the mutual inductance performance of the proposed system, the vector magnetic potential approach is utilized to determine the mutual inductance of two rectangular coils [23, 28]. Figure 2 depicts the layout of two single-turn rectangular coils with general dimensions, in which $a_1$ and $a_2$ correspond to the semi-length and semi-width of the transmitter coil's inner diameter, respectively, while $b_1$ and $b_2$ represent the semi-length and semi-width of the receiver coil's inner diameter, respectively. Here, $s_1$ indicates the axial offset from the center $O_1$ of $\text{Coil}_1$ to the coordinate origin $O$, and $s_2$ denotes the corresponding vertical displacement from $O_2$ of $\text{Coil}_2$ to point $O$. $I$ indicates the current flowing through $\text{Coil}_1$. They are the key parameters required for calculating mutual inductance between coils.

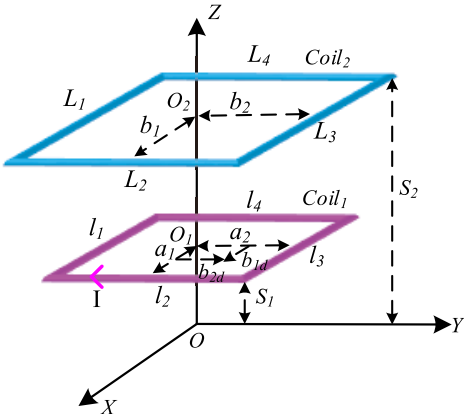


**FIGURE 2**. Schematic diagram of dual rectangular coils.

In free space, the vector magnetic potential **A** produced by a current-carrying conductor with current density **J** at an arbitrary spatial point $P(x, y, z)$ is given by:

$$\mathbf{A}(x, y, z) = \frac{\mu_0}{4\pi} \int_v \frac{\mathbf{J}(x', y', z')\mathrm{d}v'}{R} \tag{1}$$

In Equation (1), $v$ corresponds to the current distribution within the conductor, $\mu_0$ the magnetic permeability of vacuum, and $R$ the distance between an arbitrary location $P(x, y, z)$ and the source point located at $(x', y', z')$, which is formulated as:

$$R = \sqrt{(x - x')^2 + (y - y')^2 + (z - z')^2} \tag{2}$$

By applying the Fourier and inverse Fourier transforms to solve Equation (1), the resulting expression for the transformed vector magnetic potential is obtained:

$$\mathbf{a}(\xi,\eta,z) = \frac{\mu_0}{2}\int_v \frac{1}{q}\mathrm{e}^{-\mathrm{j}(x'\xi+y'\eta)}\cdot\mathbf{J}(x',y',z') \cdot\mathrm{e}^{-q|z-z'|}\mathrm{d}v' \tag{3}$$

In this expression, $\xi$ and $\eta$ represent the dual Fourier transform variables, with $q^2 = \xi^2 + \eta^2$. The incident magnetic flux density is related to the magnetization vector through the following expression:

$$\mathbf{B} = \nabla\times\mathbf{A} = \mathbf{a}_x\left(\frac{\partial A_z}{\partial y} - \frac{\partial A_y}{\partial z}\right) +\mathbf{a}_y\left(\frac{\partial A_x}{\partial z} - \frac{\partial A_z}{\partial x}\right) + \mathbf{a}_z\left(\frac{\partial A_y}{\partial x} - \frac{\partial A_x}{\partial y}\right) \tag{4}$$

where $\nabla$ denotes the Hamilton operator, and $\mathbf{A}$ represents the vector magnetic potential. Through double Fourier transform operations and computational analysis, the magnetic flux density expression can be further derived as:

$$\begin{cases} B_x(x,y,z) = \frac{1}{4\pi^2}\int_{-\infty}^{\infty}\int_{-\infty}^{\infty} b_x\cdot\mathrm{e}^{\mathrm{j}(x\xi+y\eta)}\mathrm{d}\xi\mathrm{d}\eta \\ B_y(x,y,z) = \frac{1}{4\pi^2}\int_{-\infty}^{\infty}\int_{-\infty}^{\infty} b_y\cdot\mathrm{e}^{\mathrm{j}(x\xi+y\eta)}\mathrm{d}\xi\mathrm{d}\eta \\ B_z(x,y,z) = \frac{1}{4\pi^2}\int_{-\infty}^{\infty}\int_{-\infty}^{\infty} b_z\cdot\mathrm{e}^{\mathrm{j}(x\xi+y\eta)}\mathrm{d}\xi\mathrm{d}\eta \end{cases} \tag{5}$$

According to Equation (5), the expression for mutual inductance between $\mathrm{Coil}_1$ and $\mathrm{Coil}_2$ is given as follows:

$$M_{12} = \frac{1}{4\pi^2 I}\int_{-\infty}^{\infty}\int_{-\infty}^{\infty}(C_{ix}+C_{iz}) \cdot\frac{\mathrm{e}^{\mathrm{j}(b_{1d}+b_1)\xi} - \mathrm{e}^{\mathrm{j}(b_{1d}-b_1)\xi}}{\mathrm{j}\xi} \cdot\frac{\mathrm{e}^{\mathrm{j}(b_{2d}+b_2)\eta} - \mathrm{e}^{\mathrm{j}(b_{2d}-b_2)\eta}}{\mathrm{j}\eta}\cdot\mathrm{e}^{-qs_2}d\xi d\eta \tag{6}$$

$b_{1d}$ and $b_{2d}$ represent the offsets along the $x$-axis and $y$-axis, respectively. The expressions for $C_{ix}$ and $C_{iz}$ are as follows:

$$\begin{aligned} C_{ix} &= \frac{-\mathrm{j}2\mu_0 I\sin(\xi a_1)\sin(\eta a_2)}{\eta}\mathrm{e}^{s_1 q} \\ C_{iz} &= \frac{-2\mu_0 I q\sin(\xi a_1)\sin(\eta a_2)}{\xi}\mathrm{e}^{s_1 q} \end{aligned} \tag{7}$$

Equation (8) can be employed to compute the mutual inductance existing among the various turns of a coil:

$$M = \sum_{m=1}^{N_1}\sum_{n=1}^{N_2} M_{mn} \tag{8}$$

In this expression, $N_1$ and $N_2$ indicate the number of turns in $\mathrm{Coil}_1$ and $\mathrm{Coil}_2$, respectively, while $m$ and $n$ correspond to the $m$th turn of $\mathrm{Coil}_1$ and the $n$th turn of $\mathrm{Coil}_2$. Based on the above formula, MATLAB can efficiently calculate the mutual inductance between any rectangular coils. Compared to Ansys finite element software simulations, this method offers significantly higher computational speed, providing a theoretical basis for subsequent mutual inductance optimization. This rapid calculation advantage is particularly evident during system design and debugging.

### 2.2. RSMIC Structural Design

To accommodate the large maximum offset distance between coupling coils in dynamic wireless charging while maintaining quasi-constant mutual inductance within this range, this paper proposes an RSMIC coil structure, with a three-dimensional schematic shown in Figure 3. The receiving coil $Rx$ comprises three layers: the bottom layer is a single large rectangular main receiving coil ($Rxa$); the middle layer consists of two identical, vertically symmetrical small rectangular gain coils ($Rxb1$ and $Rxb2$); and the top layer is a small rectangular anti-series suppression coil ($Rxc$). $Rxa$, $Rxb1$, and $Rxb2$ are connected in series in the same direction and then in series in the opposite direction with $Rxc$ to form a large receiving coil $Rx$. $Tx$ is formed by three coils connected in series in the same direction: $Txa$ is the central square main transmitting coil, while $Txb1$ and $Txb2$ are adjacent and vertically symmetrical, located in the second layer as transmitting gain coils. Both $Tx$ and $Rx$ are symmetrical about the origin center. $h_{Rxa\text{-}o}$ denotes the external height of $Rxa$, while $l_{Rxa\text{-}o}$ represents its external width. $h_{Rxa\text{-}i}$ indicates the internal height of $Rxa$, and $l_{Rxa\text{-}i}$ denotes its internal width. Similar dimensional notation applies to other coils. Figure 4 illustrates the dimensional layout of each coil.

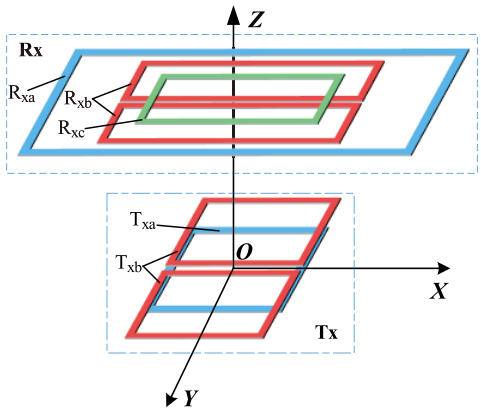


**FIGURE 3**. Three-dimensional schematic diagram of coil.

Compared to traditional coil structures, RSMIC configuration exhibits the following characteristics. First, the primary transmitter side $Tx$ dimensions are smaller than the secondary receiver side $Rx$ dimensions within the coupling mechanism, reducing mutual inductance fluctuation rates. Second, the receiver coil comprises four coils while the transmitter coil consists of three coils, enhancing inter-coil interactions and strengthening mutual inductance values. Finally, the top layer of the receiving coil employs a reverse-series configuration, with two DD coils symmetrically positioned on both sides of the receiving and transmitting coils. This effectively balances

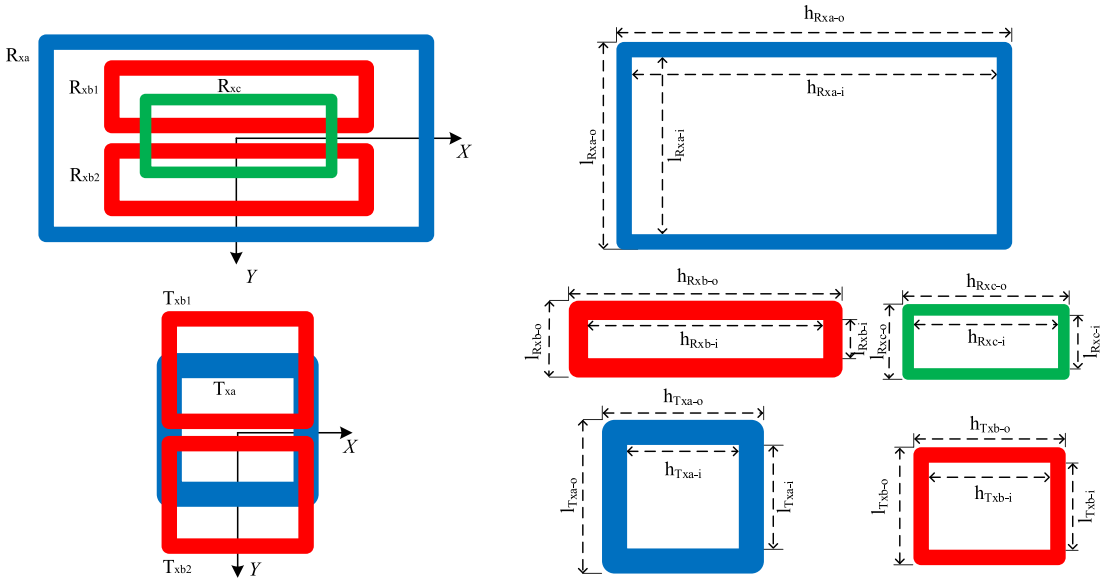


**FIGURE 4**. Schematic diagram of coil dimensions.

mutual inductance variations. In summary, when the receiving coil shifts within 55% of the transmitting coil's outer diameter along the $X$-axis, mutual inductance changes occur between each small coil in the transmitting coil and each small coil in the receiving coil. However, the overall mutual inductance variation remains minimal.

The mutual inductance between the RSMIC-structured transmitter and receiver coils is calculated using Neumann's formula, as shown in Equation (9).

$$\begin{aligned} M_{Tx\text{-}Rx} \;=\; & M_{Txa\text{-}Rxa} + M_{Txa\text{-}Rxb1} + M_{Txa\text{-}Rxb2} \\ & - M_{Txa\text{-}Rxc} + M_{Txb1\text{-}Rxa} + M_{Txb1\text{-}Rxb1} \\ & + M_{Txb1\text{-}Rxb2} - M_{Txb1\text{-}Rxc} + M_{Txb2\text{-}Rxa} \\ & + M_{Txb2\text{-}Rxb1} + M_{Txb2\text{-}Rxb2} - M_{Txb2\text{-}Rxc} \end{aligned} \quad (9)$$

$M_{Tx\text{-}Rx}$ signifies the mutual inductance for the entire transmitter-receiver pair. Meanwhile, $M_{Txa\text{-}Rxa}$ indicates the mutual inductance specifically between the primary coil of the transmitter ($Txa$) and the primary coil of the receiver ($Rxa$). Other symbols follow the same convention. Based on the structural characteristics of rectangular coils and mutual inductance calculation methods [23], the following patterns emerge from analysis. When the receiving coil shifts along the positive $X$-axis direction, the mutual inductances $M_{Tx\text{-}Rxa}$, $M_{Tx\text{-}Rxb1}$, $M_{Tx\text{-}Rxb2}$ decrease, while the mutual inductance with $M_{Tx\text{-}Rxc}$ increases. Therefore, as long as the reduction in the former equals the increase in the latter, the mutual inductance value in the $X$-direction can be maintained as a quasi-constant.

Based on the mutual inductance calculation formula, an analysis of the mutual inductance changes between the coils in the RSMIC arrangement is conducted, as depicted in Figure 5. When the transmitting and receiving coils are both displaced in the positive $X$-axis direction, mutual inductance $M_{Tx\text{-}Rxa}$ first increases and then decreases. The mutual inductance $M_{Tx\text{-}Rxb}$ decreases with increasing distance, while $M_{Tx\text{-}Rxc}$ increases with distance. Meanwhile, $M_{Tx\text{-}Rx}$ remains essentially constant. Therefore, by adjusting coil parameters, the mutual inductance at the offset point can be modified to ensure that the total mutual inductance $M_{Tx\text{-}Rx}$ between the transmitter and receiver coils achieves a quasi-constant state.

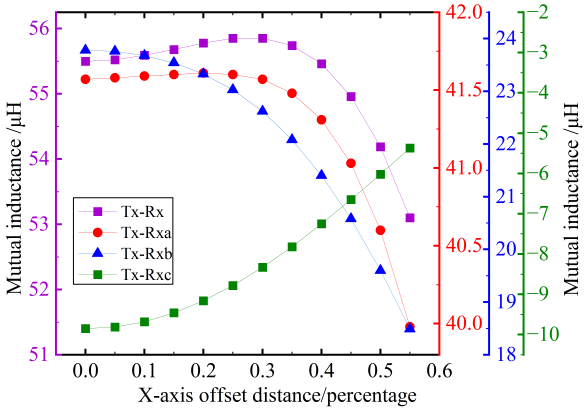


**FIGURE 5**. Mutual inductance characteristics during RSMIC coil offset process.

## 3. RSMIC STRUCTURE OPTIMIZATION

Mutual inductance, which serves as a critical measure of the magnetic coupling intensity between the transmitting and receiving coils, governs the overall efficiency of the power transfer process, and an increase in the mutual inductance coupling coefficient leads to improved efficiency. To enhance mutual inductance stability, we propose an optimization method based on minimizing mutual inductance fluctuations. The core principle involves adjusting the shape or dimensions of coils and cores to minimize fluctuation rates under varying misalignments while meeting size constraints. Through mutual inductance optimization, the resulting core-integrated coil assemblies maintain stable performance across diverse practical applications.

**TABLE 1**. Coil parameter optimization range.

| Parameter | Value | Parameter | Value | Parameter | Value |
|---|---|---|---|---|---|
| $l_{Txa-i}$/mm | $180 \sim 220$ | $h_{Txa-i}$/mm | $180 \sim 220$ | $N_{Txa}$ | $15 \sim 20$ |
| $l_{Txb-i}$/mm | $100 \sim 150$ | $h_{Txb-i}$/mm | $180 \sim 220$ | $N_{Txb}$ | $15 \sim 20$ |
| $l_{Rxa-i}$/mm | $260 \sim 300$ | $h_{Rxa-i}$/mm | $660 \sim 700$ | $N_{Rxa}$ | $10 \sim 15$ |
| $l_{Rxb-i}$/mm | $20 \sim 60$ | $h_{Rxb-i}$/mm | $478 \sim 508$ | $N_{Rxb}$ | $10 \sim 15$ |
| $l_{Rxc-i}$/mm | $160 \sim 200$ | $h_{Rxc-i}$/mm | $360 \sim 400$ | $N_{Rxc}$ | $3 \sim 6$ |

### 3.1. RSMIC Coil Structure Optimization

This section proposes a method for achieving quasi-constant mutual inductance by optimizing coil parameters, with optimization results obtained using MATLAB calculations. Based on the rectangular coil mutual inductance calculation method, the mutual inductance of the RSMIC coil structure can be computed. This paper sets mutual inductance $M$ as the optimization objective and optimizes the RSMIC structural parameters according to the principle of minimizing mutual inductance fluctuation to achieve fundamentally constant mutual inductance. First, coil parameters are optimized to determine their optimal data matrix. Building upon this, core dimensions are further adjusted to enhance overall performance.

(1) Objective Function

Under fixed conditions of vertical distance between transmitter and receiver coils, inter-turn spacing, and wire diameter, analyze and optimize the key parameters affecting mutual inductance $M$. Specifically, optimize the length, width, and number of turns for both transmitter and receiver coils.

$$M = f\begin{pmatrix} l_{Txa-i}, h_{Txa-i}, N_{Txa}, l_{Txb-i}, \\ h_{Txb-i}, N_{Txb}, l_{Rxa-i}, h_{Rxa-i}, \\ N_{Rxa}, l_{Rxb-i}, h_{Rxb-i}, N_{Rxb}, \\ l_{Rxc-i}, h_{Rxc-i}, N_{Rxc} \end{pmatrix} \tag{10}$$

(2) Setting Constraints

As shown in Equation (10), the mutual inductance $M$ of the coil is related to its dimensions and number of turns. During optimization, smaller step sizes for the side length yield more data points in MATLAB that meet the requirements. Based on practical considerations and to reduce redundant data, the following constraints are set: $l_{Txa-i} = h_{Txa-i} = h_{Txb-i}$, $N_{Txa} = N_{Txb}$, $N_{Rxa} = N_{Rxb}$. It means that the inner length and width of the transmit main coil $Txa$ are equal and identical to the inner width of the transmit gain coil $Txb$, and the two coils feature an identical turn count. Similarly, the primary receiving coil $Rxa$ and receiver booster coil $Rxb$ possess an equal number of windings. The inner diameter increment is 10 mm, and the turn increment is 1 turn. The ranges for the parameters to be optimized are provided in Table 1.

(3) Coil Parameter Optimization

Based on the principle of minimizing mutual inductance fluctuation, the RSMIC structure undergoes parameter optimization. The mutual inductance value and fluctuation rate under offset conditions are calculated. After verifying compliance with requirements, the coil dimensions are optimized. The maximum and minimum mutual inductance fluctuation rates when the coil is offset along the $X$-axis are defined as $\varepsilon_{x1}$ and $\varepsilon_{x2}$, respectively. The formula is given by Equation (11):

$$\begin{cases} \varepsilon_{x1} = \frac{M_{\max\_X} - M_0}{M_0} \\ \varepsilon_{x2} = \frac{|M_{\min\_X} - M_0|}{M_0} \end{cases} \tag{11}$$

$M_0$ denotes the mutual inductance between coils when aligned. $M_{\max\_X}$ and $M_{\min\_X}$ represent the maximum and minimum mutual inductance between coils when shifted in the $X$-direction, respectively. The coil parameter optimization process based on the principle of minimizing mutual inductance fluctuation is illustrated in Figure 6. The coil optimization procedure is as follows: First, initial parameters such as transmission distance, copper wire diameter, and mutual inductance fluctuation threshold are set. $\varepsilon^*_{x1}$, $\varepsilon^*_{x2}$ are both set to 5%. The optimization ranges for the inner length, inner width, and number of turns within each coil, as determined in Table 1, are applied as constraints. Subsequently, the optimization parameters are traversed to calculate the mutual inductance values $M_x$ and mutual inductance fluctuation rates $\varepsilon_{x1}$, $\varepsilon_{x2}$ under different offset conditions. The system checks whether $\varepsilon_{x1}$ is less than $\varepsilon^*_{x1}$ and whether $\varepsilon_{x2}$ is less than $\varepsilon^*_{x2}$. If both conditions are met, the parameter matrix is saved; otherwise, the next set of parameters is traversed. If parameters exceed the range, the compliant parameter matrix is similarly saved. Finally, after traversing all parameters, the process terminates and outputs the coil parameter matrix that meets the requirements.

The final geometrical parameters for the coils on both the transmitter and receiver sides are summarized in Table 2. Results demonstrate that the optimized coil parameters effectively maintain mutual inductance between coil structures, enhancing overall energy transfer efficiency and reliability.

### 3.2. Core Optimization

After determining the RSMIC coil dimensions, a core parameter optimization strategy based on minimizing mutual inductance fluctuations was proposed to address severe fluctuation issues caused by coil misalignment. This approach entails the optimization of multiple variables, including geometrical size, inter-slot distance, and the quantity and morphology of slots within the transmitter and receiver cores.

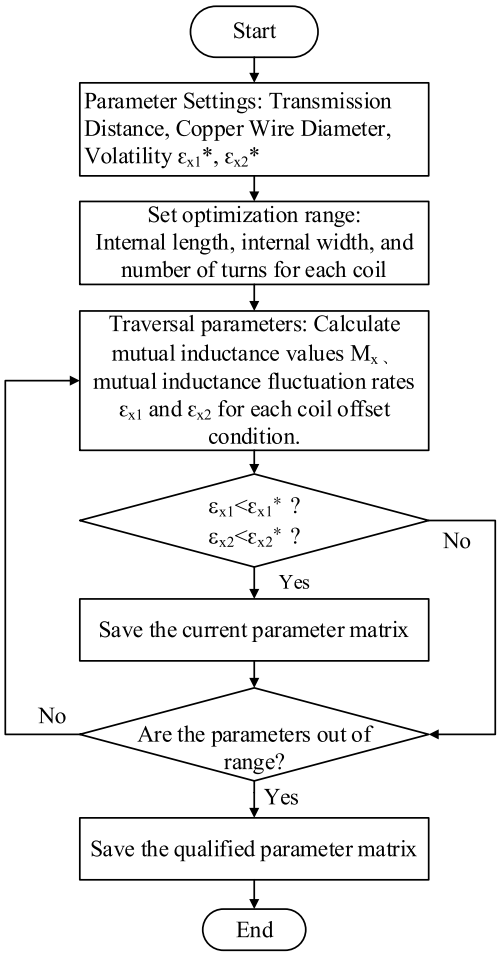


**FIGURE 6**. Coil optimization flowchart.

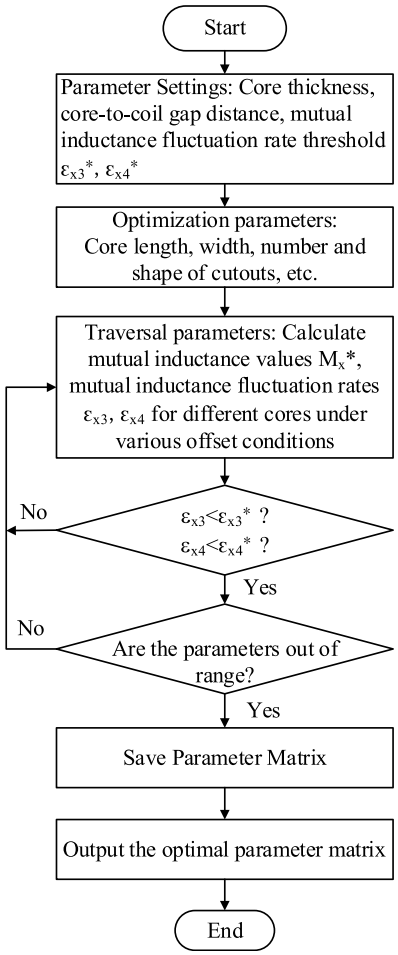


**FIGURE 7**. Magnetic core optimization flowchart.

**TABLE 2**. Coil parameter optimization results.

| Parameter | Value | Parameter | Value | Parameter | Value |
|---|---|---|---|---|---|
| $l_{Txa-i}$/mm | 200 | $h_{Txa-i}$/mm | 200 | $N_{Txa}$ | 17 |
| $l_{Txb-i}$/mm | 130 | $h_{Txb-i}$/mm | 200 | $N_{Txb}$ | 17 |
| $l_{Rxa-i}$/mm | 280 | $h_{Rxa-i}$/mm | 680 | $N_{Rxa}$ | 13 |
| $l_{Rxb-i}$/mm | 40 | $h_{Rxb-i}$/mm | 498 | $N_{Rxb}$ | 13 |
| $l_{Rxc-i}$/mm | 180 | $h_{Rxc-i}$/mm | 380 | $N_{Rxc}$ | 5 |

(1) Core Parameter Configuration: The transmitter-side core is mounted on the coil base, while the receiver-side core is fixed atop the coil. Fundamental core parameters are set as follows: core thickness 10 mm, core-to-coil gap approximately zero, mutual inductance fluctuation rate thresholds $\varepsilon_{x3}^*$ and $\varepsilon_{x4}^*$ both set to 5%. Core parameters are configured to match coil dimensions, establishing foundational conditions for subsequent optimization.

(2) Defining the Optimization Scope: Based on the optimized coil structure, select the core structure and establish the parameter ranges for core optimization, such as core length, width, number and shape of cutouts. Clearly define the optimization direction and boundaries to ensure that the optimization process proceeds according to established rules.

(3) Core Parameter Optimization: Use ANSYS simulation software to calculate the mutual inductance values $M_x^*$ for different cores under various offset conditions. Calculate the maximum and minimum mutual inductance fluctuation rates $\varepsilon_{x3}$ and $\varepsilon_{x4}$ using Equation (12). Determine whether $\varepsilon_{x3}$ is less than $\varepsilon_{x3}^*$ and $\varepsilon_{x4}$ less than $\varepsilon_{x4}^*$. If satisfied, save the parameter matrix. If unsatisfied but parameters remain within bounds, proceed to the next parameter set. Continue iterating until all parameters are evaluated, ultimately outputting the optimal core

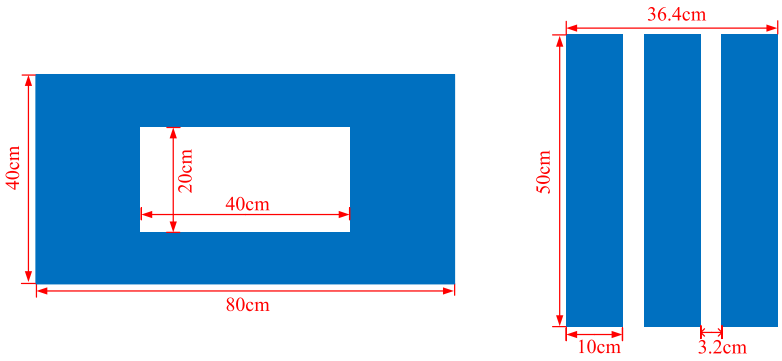


**FIGURE 8**. Optimized core dimensions.

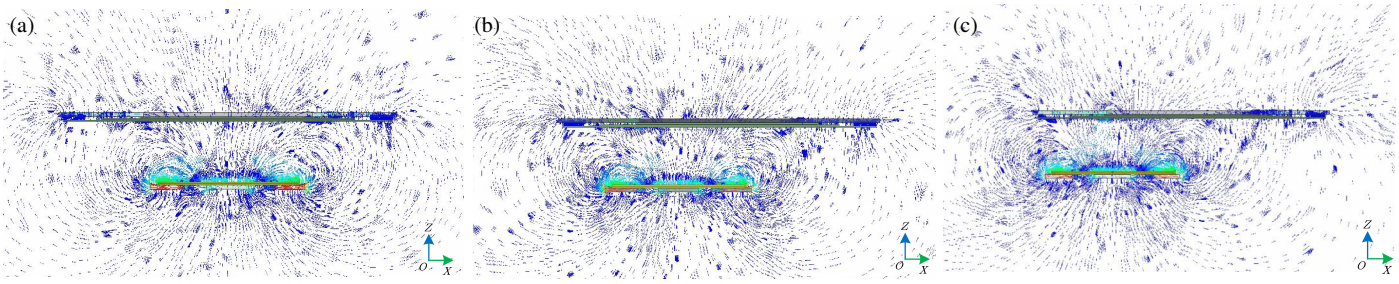


**FIGURE 9**. Magnetic field distribution diagram when the RSMIC structure is displaced. (a) $\Delta X = 0$, (b) $\Delta X = 0.3h_{Tx}$, (c) $\Delta X = 0.55h_{Tx}$.

parameter matrix meeting requirements.

$$\begin{cases} \varepsilon_{x3} = \dfrac{M^*_{\text{max\_}X} - M^*_0}{M^*_0} \\ \varepsilon_{x4} = \dfrac{\left|M^*_{\text{min\_}X} - M^*_0\right|}{M^*_0} \end{cases} \tag{12}$$

$M^*_0$ denotes the mutual inductance between coils after core offset matching. $M^*_{\text{max\_}X}$ and $M^*_{\text{min\_}X}$ represent the maximum and minimum mutual inductances between coils after core addition during $X$-direction offset, respectively. The core parameter optimization process is shown in Figure 7, with the optimized core dimensions depicted in Figure 8. The core thickness is 10 mm. The transmit coil core consists of three identical strip cores arranged in parallel. The transmitting coil core is composed of three identical strip cores arranged in parallel. Specifically, this core has a length of 50 cm and a width of 10 cm, with its total outer width slightly exceeding that of the transmitting coil and its outer length slightly shorter than that of the transmitting coil. The receiving coil employs a mesh core. This mesh core is formed by cutting a small rectangle (40 cm long $\times$ 20 cm wide) from the center of an outer large rectangle (80 cm long $\times$ 40 cm wide). Compared to a fully filled core, this design saves 22.31% of core material while maintaining efficiency and ensuring quasi-constant mutual inductance during horizontal displacement.

A simulation model of the optimized core-equipped RSMIC coil structure was created using Ansys finite element software. Field strength values and magnetic flux line orientations were recorded as displacement distance varied. As shown in Figure 9, magnetic field distribution diagrams corresponding to three different offset distances were recorded. Analysis of the magnetic field distribution reveals that magnetic field lines become denser with smaller offset distances and relatively looser with larger offsets. However, the overall variation in magnetic field density remains minimal after optimization, demonstrating the effectiveness of the magnetic core optimization.

## 4. EXPERIMENTAL VALIDATION

### 4.1. Experimental Setup

In order to verify the performance of the designed RSMIC-based wireless power transfer system, a corresponding prototype was constructed using coil and core dimensions derived from mutual inductance optimization. The overall experimental setup comprised a DC power supply, inverter module, transmitter coil, transmitter-side compensation capacitor ($C_{S1}$), receiver coil, receiver-side compensation capacitor ($C_{S2}$), rectifier module, magnetic core, and terminal load. The experiment employed an $S$-$S$ topology circuit, with the inverter and rectifier modules implemented using silicon carbide MOSFETs (C3M0075120D). Self-inductance and mutual inductance were measured using an IM3536 impedance analyzer. The coils employed 0.1 mm $\times$ 800-strand Litz wire, set at a 15 cm transmission distance with a resonant frequency of 85 kHz. Figure 10 shows the overall experimental setup, and Figure 11 displays simulation models of the coil structures with and without magnetic cores.

The primary system parameters are summarized in Table 3. Initially, the mutual inductance computation approach from [23] was utilized in MATLAB to determine the calculated mutual inductance $M_c$ of the RSMIC configuration. Subsequently, Ansys finite element software was utilized

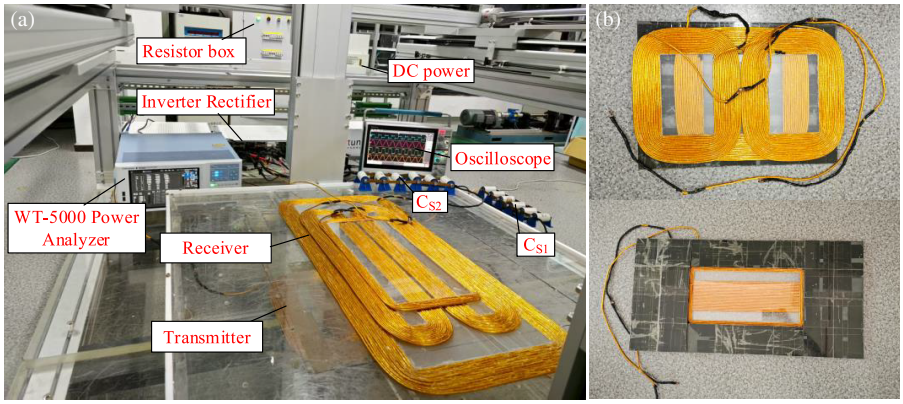


**FIGURE 10**. Experimental setup. (a) Overall experimental diagram of the system. (b) Diagram of the magnetic core coupling coil.

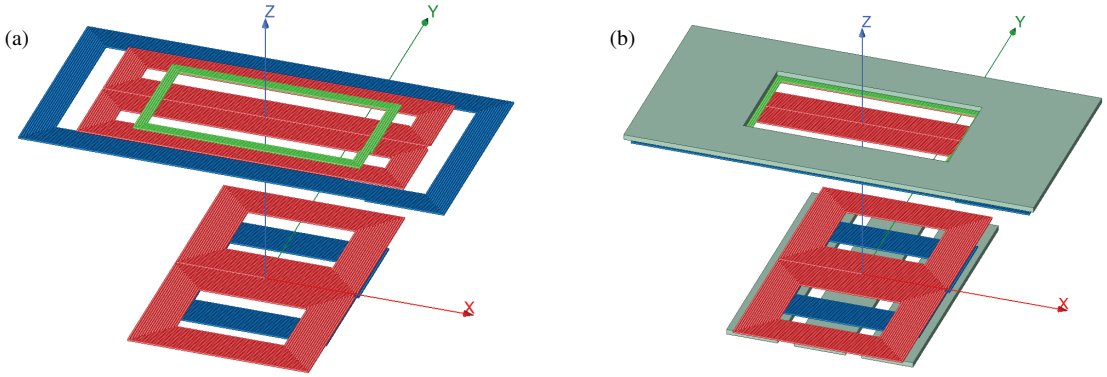


**FIGURE 11**. Ansys simulation model. (a) Core-less simulation model. (b) Magnetic core simulation model.

**TABLE 3**. System parameters of the RSMIC-based WPT system.

| Parameter | Physical meaning | Value |
|---|---|---|
| $L_1/\mu H$ | Self-inductance of the transmitting coil | 442.65 |
| $L_1^*/\mu H$ | Self-inductance of the transmitting coil with core | 721.82 |
| $L_2/\mu H$ | Self-inductance of the receiving coil | 420.90 |
| $L_2^*/\mu H$ | Self-inductance of the receiving coil with core | 629.60 |
| $C_1/nF$ | Compensation capacitance of the transmitting coil | 7.92 |
| $C_1^*/nF$ | Compensation capacitance of the transmitting coil with core | 4.86 |
| $C_2/nF$ | Compensation capacitance of the receiving coil | 8.33 |
| $C_2^*/nF$ | Compensation capacitance of the receiving coil with core | 5.57 |
| $R_1/\Omega$ | Parasitic resistance of the transmitting coil | 0.106 |
| $R_2/\Omega$ | Parasitic resistance of the receiving coil | 0.143 |
| $f_0/Hz$ | Working frequency | 85000 |
| $R_L/\Omega$ | Load resistance | 33 |
| $R_L^*/\Omega$ | Load resistance with core | 50 |

for simulation to extract the simulated mutual inductance value $M_s$ of this structure, with the simulation model shown in Figure 11. Finally, the experimental values of the coil self-inductance and mutual inductance, denoted as $M_e$, were measured using an IM3536 impedance analyzer. The errors between the simulated and calculated mutual inductance values relative to the experimental values are defined as $\varepsilon_s$ and $\varepsilon_c$, respectively. Their expressions are as follows:

$$\begin{aligned} \varepsilon_s &= \left| \frac{M_s - M_e}{M_e} \right| \times 100\% \\ \varepsilon_c &= \left| \frac{M_c - M_e}{M_e} \right| \times 100\% \end{aligned} \tag{13}$$

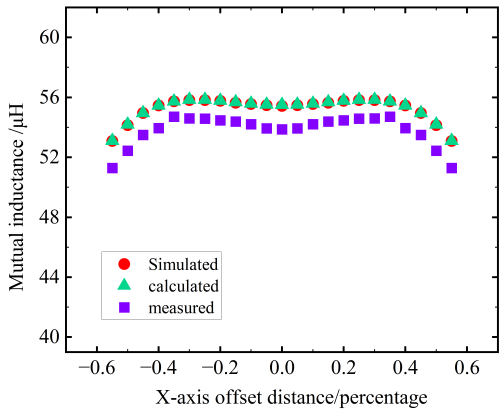


**FIGURE 12**. Variation curve of mutual inductance for a core-less coil.

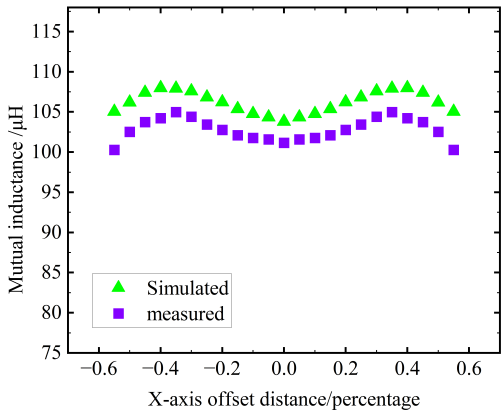


**FIGURE 13**. Curve of mutual inductance change in a core-type coil.

**TABLE 4**. Mutual inductance and error data for RSMIC coil (Core-less).

| misalignment/mm | $M_c$/μH | $M_s$/μH | $M_e$/μH | $\varepsilon_{ce}$/% | $\varepsilon_{se}$/% |
|---|---|---|---|---|---|
| 0 | 55.5 | 55.42 | 53.86 | 3.04% | 2.90% |
| 16.8 | 55.52 | 55.48 | 53.94 | 2.93% | 2.86% |
| 33.6 | 55.59 | 55.55 | 54.21 | 2.55% | 2.47% |
| 50.4 | 55.68 | 55.64 | 54.39 | 2.37% | 2.30% |
| 67.2 | 55.78 | 55.77 | 54.47 | 2.40% | 2.39% |
| 84.0 | 55.85 | 55.82 | 54.59 | 2.31% | 2.25% |
| 100.8 | 55.85 | 55.82 | 54.6 | 2.29% | 2.23% |
| 117.6 | 55.74 | 55.74 | 54.71 | 1.88% | 1.88% |
| 134.4 | 55.46 | 55.46 | 53.95 | 2.80% | 2.80% |
| 151.2 | 54.96 | 54.96 | 53.49 | 2.75% | 2.75% |
| 168.0 | 54.19 | 54.14 | 52.44 | 3.34% | 3.24% |
| 184.8 | 53.1 | 53.09 | 51.28 | 3.55% | 3.53% |

## 4.2. Mutual Inductance Verification

### 4.2.1. Verification of Mutual Induction in Coreless RSMIC Structure

Table 4 presents the calculated mutual inductance $M_c$, simulated value $M_s$, experimental value $M_e$, and their errors for RSMIC under $X$-axis offset. Errors $\varepsilon_{ce}$ and $\varepsilon_{se}$ are below 3.55% and 3.53%, respectively, validating the accuracy of the proposed calculation method and optimization approach. Figure 12 (based on Table 4) shows that mutual inductance varies in a wave-like pattern with offset distance: 53.86 μH at 0 mm, 54.71 μH (maximum) at 117.6 mm, and 51.28 μH (minimum) at 184.8 mm. Using Equation (11), $\varepsilon_{x1} = 1.58\%$ and $\varepsilon_{x2} = 4.79\%$, indicating stable mutual inductance against distance variation. This differs from other structures with monotonically decreasing characteristics, achieving quasi-constant mutual inductance.

### 4.2.2. Verification of Mutual Induction with Magnetic Core RSMIC Structure

Table 5 presents the simulated mutual inductance $M_s$, experimental value $M_e$, and error for core-equipped RSMIC under $X$-axis offset. The maximum error $\varepsilon_{se}$ is only 3.85%, validating the efficacy of the proposed core design optimization method. Figure 13 (based on Table 5) shows that mutual inductance varies similarly to the coreless configuration: 101.15 μH at 0 mm, 104.98 μH (maximum) at 117.6 mm, and 100.27 μH

**TABLE 5**. Mutual inductance and error data for RSMIC coil (Core-equipped).

| misalignment/mm | $M_s$/μH | $M_e$/μH | $\varepsilon_{se}$/% |
|---|---|---|---|
| 0 | 103.81 | 101.15 | 2.63% |
| 16.8 | 104.33 | 101.58 | 2.71% |
| 33.6 | 104.77 | 101.76 | 2.96% |
| 50.4 | 105.39 | 102.09 | 3.23% |
| 67.2 | 106.23 | 102.78 | 3.36% |
| 84.0 | 106.82 | 103.44 | 3.27% |
| 100.8 | 107.6 | 104.39 | 3.08% |
| 117.6 | 107.93 | 104.98 | 2.81% |
| 134.4 | 107.99 | 104.21 | 3.63% |
| 151.2 | 107.4 | 103.74 | 3.53% |
| 168.0 | 106.19 | 102.52 | 3.58% |
| 184.8 | 105.03 | 100.27 | 3.85% |

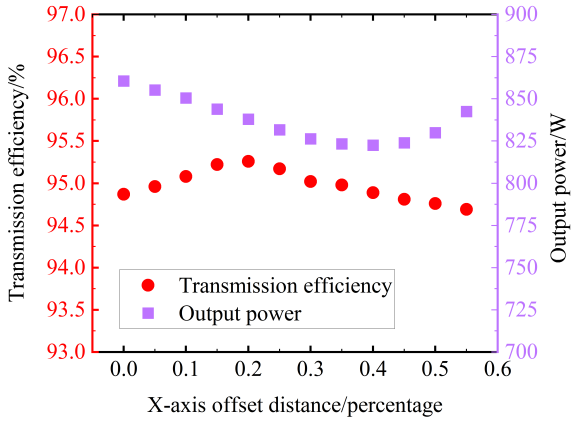


**FIGURE 14**. Output power and transmission efficiency of the RSMIC structure.

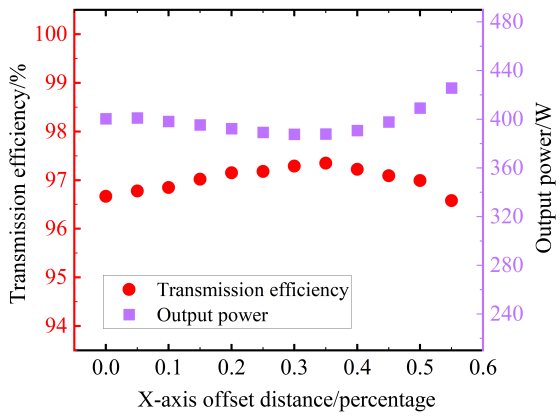


**FIGURE 15**. Output power and transmission efficiency of core-based RSMIC structure.

**TABLE 6**. Comparison of anti-offset performance in wireless power transfer systems.

| Ref. | Coil Structure | Transmission Distance/mm | Maximum Maximum Offset Distance/mm | Offset Rate/% | Fluctuation Rate/% | Output Power/W | with Magnetic Core |
|---|---|---|---|---|---|---|---|
| [25] | DQDD | 130 | 150 | 38.4 | 55 | 500 | YES |
| [26] | ISC | 150 | 225 | 50 | 3.81 | 108.8 | NO |
| [27] | Flat Solenoid | 170 | 120 | 40 | 12.3 | 500 | YES |
| Our work | RSMIC | 150 | 184.8 | 55 | 4.79 | 860.64 | YES |

(minimum) at 184.8 mm. Using Equation (12), $\varepsilon_{x3} = 3.79\%$ and $\varepsilon_{x4} = 0.87\%$, indicating that the RSMIC with perforated core achieves quasi-constant mutual inductance.

### 4.3. Output Power and Transmission Efficiency

To further evaluate the output power and efficiency of the RSMIC structure at different offset distances, a wireless power transfer system was established. The experimental setup is shown in Figure 10, where the output performance of both coreless and core-equipped RSMIC coils was successively verified.

#### 4.3.1. Cores-Free Power

Figure 14 shows the output power and transmission efficiency of the RSMIC structure at different offset distances. Experimental findings demonstrate that under perfect coil alignment, the system reaches an output power of 860.64 W with a transmission efficiency of 94.87%. When the offset distance is within 55% of the transmitter coil's outer diameter (184.8 mm), the maximum and minimum output powers are 860.64 W and 822.58 W, respectively, while the maximum and minimum transmission efficiencies are 95.26% and 94.69%. The maximum fluctuation rates for output power and transmission efficiency were 4.42% and 0.41%, respectively. During $X$-axis displacement, the system's transmission efficiency exhibited a trend of initial increase followed by decrease, consistent with the mutual inductance variation shown in Figure 12. Results indicate that the transmission efficiency fluctuation rate of the RSMIC structure remains minimal during displacement. This is attributed to the near-constant mutual inductance within this configuration.

#### 4.3.2. Core Power

Figure 15 shows the output power and transmission efficiency of the core-based RSMIC structure at different offset distances. Experimental results indicate that when the coils are perfectly aligned, the system achieves an output power of 400.55 W and a transmission efficiency of 96.67%. When the offset distance is within 55% of the outer diameter length of the transmitter coil (184.8 mm), the maximum and minimum output powers are 401.12 W and 387.78 W, respectively, while the maximum and minimum transmission efficiencies are 97.35% and 96.58%. The maximum fluctuation rates for output power and transmission efficiency are 6.27% and 0.70%, respectively. The results indicate that the transmission efficiency fluctuation rate of the core-based RSMIC remains minimal during coil misalignment. This is attributed to the near-constant mutual inductance within the core-based RSMIC structure throughout the misalignment period.

### 4.4. Comparison of Anti-Offset Performance

Table 6 presents a performance comparison with three typical anti-offset coil structures. From the comparison, it can be seen that our RSMIC performs excellently in several key indicators. In terms of misalignment tolerance, its maximum offset distance ratio of 55% is higher than 38.4% of DQDD and 40% of Flat Solenoid, and comparable to 50% of ISC, indicating

a stronger lateral offset bearing capacity. In terms of mutual inductance stability, the fluctuation rate of RSMIC at 4.79% is significantly lower than 55% of DQDD and 12.3% of Flat Solenoid, and also performs well compared to 3.81% of ISC. In terms of output power, RSMIC outputs 860.64 W, exceeding 500 W of DQDD, 108.8 W of ISC, and comparable to 500 W of Flat Solenoid, demonstrating a higher power transmission capability. In addition, RSMIC, like DQDD and Flat Solenoid, integrates a magnetic core, which contributes to the realization of its performance advantages, while ISC does not. Overall, these comparisons confirm that our RSMIC is a more competitive solution in dynamic wireless charging applications, achieving a good balance in wide misalignment tolerance, stable mutual inductance, and high output power.

## 5. CONCLUSION

To enhance system offset immunity, this paper proposes a reverse series multilayer interactive coil (RSMIC) structure. Structural characteristics and mutual inductance properties of RSMIC are analyzed, followed by an optimization strategy based on vector magnetic potential for mutual inductance calculation, optimizing coil and core parameters to minimize mutual inductance fluctuations. Prototype experiments validate the method: with $X$-direction displacement within 55% (184.8 mm) of the transmitter outer diameter, RSMIC maintains mutual inductance fluctuation below 5% with or without the core. The core increases maximum mutual inductance from 54.71 µH to 104.98 µH and maximum efficiency from 95.26% to 97.35%. The core-optimized RSMIC is highly suitable for smart rail dynamic wireless charging, excelling in offset tolerance and efficiency. Future work will focus on $Y$-direction offset resistance enhancements.

## ACKNOWLEDGEMENT

This research received funding from the Hunan Provincial Natural Science Foundation (2022JJ30226), the National Key R&D Program (2022YFB3403200), the Key Project of the Hunan Provincial Department of Education (23A0432), and the Outstanding Young Scientist Research Project of the Hunan Provincial Department of Education (22B0577). Supported by the National Natural Science Foundation of China (NSFC) Youth Science Fund Project (62303178) and the Hunan Provincial Department of Education Research Fund Project (23C0182).

## REFERENCES

[1] Xue, M., Q. Yang, P. Zhang, J. Guo, Y. Li, and X. Zhang, "Application status and key issues of wireless power transmission technology," *Transactions of China Electrotechnical Society*, Vol. 36, No. 8, 1547–1568, 2021.

[2] Chen, Y., B. Yang, Y. Peng, Y. Lu, Z. Zhang, R. Mai, and Z. He, "Review of anti-misalignment technology in inductive wireless power transfer system," *Proceedings of the CSEE*, Vol. 43, No. 14, 5537–5556, 2023.

[3] Chen, K., Y. Jiang, T. Tan, *et al.*, "Research on 350 kW high power wireless power transfer system for rail transit," *Transactions of China Electrotechnical Society*, Vol. 37, No. 10, 2411–2421, 2445, 2022.

[4] Li, Z., M. Zhang, S. Huang, and J. Yi, "Design and optimization of structure of tower-type coil in wireless charging system for electric vehicles," *Progress In Electromagnetics Research B*, Vol. 85, 85–101, 2019.

[5] Hou, X., Z. Wang, Y. Su, Z. Liu, and Z. Deng, "A dual-frequency dual-load multirelay magnetic coupling wireless power transfer system using shared power channel," *IEEE Transactions on Power Electronics*, Vol. 37, No. 12, 15 717–15 727, 2022.

[6] Wu, L. and B. Zhang, "Overview of static wireless charging technology for electric vehicles: Part I," *Transactions of China Electrotechnical Society*, Vol. 35, No. 6, 1153–1165, 2020.

[7] Yan, H., Y. Chen, and S.-H. Yang, "UAV-enabled wireless power transfer with base station charging and UAV power consumption," *IEEE Transactions on Vehicular Technology*, Vol. 69, No. 11, 12 883–12 896, 2020.

[8] Cai, C., M. Saeedifard, J. Wang, P. Zhang, J. Zhao, and Y. Hong, "A cost-effective segmented dynamic wireless charging system with stable efficiency and output power," *IEEE Transactions on Power Electronics*, Vol. 37, No. 7, 8682–8700, 2022.

[9] Triviño, A., J. M. González-González, and J. A. Aguado, "Wireless power transfer technologies applied to electric vehicles: A review," *Energies*, Vol. 14, No. 6, 1547, 2021.

[10] Xu, H. and Z. Huang, "Alternately-arranged segmented transmitter pads with magnetic field complementation for suppressing power fluctuation in dynamic wireless power transfer," *IEEE Transactions on Power Electronics*, Vol. 39, No. 10, 14 091–14 102, 2024.

[11] Chu, S. Y., X. Cui, X. Zan, and A.-T. Avestruz, "Transfer-power measurement using a non-contact method for fair and accurate metering of wireless power transfer in electric vehicles," *IEEE Transactions on Power Electronics*, Vol. 37, No. 2, 1244–1271, 2022.

[12] Zhang, Y., S. Chen, X. Li, and Y. Tang, "Design of high-power static wireless power transfer via magnetic induction: An overview," *CPSS Transactions on Power Electronics and Applications*, Vol. 6, No. 4, 281–297, 2021.

[13] Budhia, M., G. Covic, and J. Boys, "A new IPT magnetic coupler for electric vehicle charging systems," in *IECON 2010 — 36th Annual Conference on IEEE Industrial Electronics Society*, 2487–2492, Glendale, AZ, USA, 2010.

[14] Budhia, M., J. T. Boys, G. A. Covic, and C.-Y. Huang, "Development of a single-sided flux magnetic coupler for electric vehicle IPT charging systems," *IEEE Transactions on Industrial Electronics*, Vol. 60, No. 1, 318–328, 2013.

[15] Zaheer, A., G. A. Covic, and D. Kacprzak, "A bipolar pad in a 10-kHz 300-W distributed IPT system for AGV applications," *IEEE Transactions on Industrial Electronics*, Vol. 61, No. 7, 3288–3301, 2014.

[16] Kim, S., G. A. Covic, and J. T. Boys, "Tripolar pad for inductive power transfer systems for EV charging," *IEEE Transactions on Power Electronics*, Vol. 32, No. 7, 5045–5057, 2017.

[17] Li, Y., J. Zhao, Q. Yang, L. Liu, J. Ma, and X. Zhang, "A novel coil with high misalignment tolerance for wireless power transfer," *IEEE Transactions on Magnetics*, Vol. 55, No. 6, 1–4, 2019.

[18] Ahmad, A., M. S. Alam, and A. A. S. Mohamed, "Design and interoperability analysis of quadruple pad structure for electric vehicle wireless charging application," *IEEE Transactions on Transportation Electrification*, Vol. 5, No. 4, 934–945, 2019.

[19] Kong, L. C., H. J. Li, B. Pan, and Y. Wang, "Research on quadruple D square coil with high misalignment tolerance for wireless power transfer," *Transactions of China Electrotechnical Society*,

Vol. 37, No. 13, 3361–3371, 2022.

[20] Mao, X., J. Lin, T. Su, and Y. Zhang, "Automatic guided vehicle wireless charging with dual receiving coils for misalignment tolerance," *IEEE Transactions on Circuits and Systems II: Express Briefs*, Vol. 71, No. 1, 336–339, 2024.

[21] Chen, Y., R. Mai, Y. Zhang, M. Li, and Z. He, "Improving misalignment tolerance for IPT system using a third-coil," *IEEE Transactions on Power Electronics*, Vol. 34, No. 4, 3009–3013, 2019.

[22] Tan, P., T. Peng, X. Gao, and B. Zhang, "Flexible combination and switching control for robust wireless power transfer system with hexagonal array coil," *IEEE Transactions on Power Electronics*, Vol. 36, No. 4, 3868–3882, 2021.

[23] Li, Z., J. Li, S. Li, Y. Yu, and J. Yi, "Design and optimization of asymmetric and reverse series coil structure for obtaining quasi-constant mutual inductance in dynamic wireless charging system for electric vehicles," *IEEE Transactions on Vehicular Technology*, Vol. 71, No. 3, 2560–2572, 2022.

[24] Liu, X., Y. P. Cao, C. Y. Xia, and L. Y. Yang, "Optimization of hybrid compensation topology and anti-offset performance of wireless power transfer system based on QRQP coil," *Transactions of China Electrotechnical Society*, Vol. 40, No. 12, 3828–3841, 2025.

[25] Xiao, H. H., Q. S. Zhou, S. X. Xiong, Y. Yang, and S. Y. Xie, "Wireless power transfer system based on double-layer quadrature double-D coupling structure with anti-misalignment and anti-deflection," *Transactions of China Electrotechnical Society*, Vol. 37, No. 16, 4004–4018, 2022.

[26] Li, Z., S. Li, J. Li, Y. Zou, and S. Huang, "Mutual inductance calculation and optimization of multi-receiver positive and negative series coil structure in dynamic wireless power transfer systems," *Transactions of China Electrotechnical Society*, Vol. 36, No. 24, 5153–5164, 2021.

[27] Wang, Y., K. X. Lu, Y. S. Yao, X. S. Liu, and D. G. Xu, "An electric vehicle (EV)-oriented wireless power transfer system featuring high misalignment tolerance," *Proceedings of the CSEE*, Vol. 39, No. 13, 3907–3916, 2019.

[28] Carretero, C., J. Acero, R. Alonso, J. M. Burdio, and F. Monterde, "Modeling mutual impedances of loaded non-coaxial inductors for induction heating applications," *IEEE Transactions on Magnetics*, Vol. 44, No. 11, 4115–4118, 2008.